Longitudinal Laminar Flow Between Cylinders Arranged in Regular Array

E. M. SPARROW and A. L. LOEFFLER, JR.

National Aeronautics and Space Administration, Lewis Research Center, Cleveland, Ohio

An analytical solution has been obtained for the longitudinal fully developed laminar flow between cylinders arranged in triangular or square array. Numerical results for the pressure drop and the friction factor are given over a wide range of spacing-to-diameter ratios. For large spacings the results can be represented by a single expression independent of the type of array. Plots are also given of velocity distributions and of the variation of the local shear stress around the periphery of a cylinder.

The increasing complexity of heat transfer and process situations which involve fluid flow has demanded the frequent use of flow passages of unusual geometrical configuration. The present investigation is concerned with one such novel configuration, namely the longitudinal flow between solid cylindrical rods which are arranged in regular array. A schematic diagram of the situation under study is shown in Figure 1. The rods may be located either in triangular or square array. The flow will be taken to be laminar and fully developed.

The aim of this analysis is to determine the pressure drop, shear stress, and velocity-distribution characteristics of the system. The starting point of this study is the basic law of momentum conservation. The resulting differential equation has been solved in an approximate, but almost exact, manner by the use of truncated trigonometric series. Results are obtained over a wide range of porosity values for both the triangular and square arrays. Heat transfer has not been considered.

The configuration under investigation has potential application in compact heat exchangers for nuclear reactors and other situations. Further the results should also be of interest in the theory of flow through unconsolidated porous beds (*1a*, *2a*).

The only related analytical work known to the authors is that of Emersleben (*3*), who considered only the square array. His rather involved solution, based on complex zeta functions, appears to be valid only at high porosities. Experiments covering a porosity range of 0.093 to 0.984 have been made by Sullivan (*4*) using parallel-oriented fibers, most of the tests being for fibers in random array. These previous investigations will be compared with the present theory in a later section.

ANALYSIS

The Governing Equation and Its General Solution

The physical principle which governs the velocity distribution in a (isothermal) flowing fluid is conservation of momentum. To translate this physical law into mathematical terms, cylindrical coordinates will be used. The derivation is facilitated by Figure 2. The conservation principle requires that under steady state conditions the net change of momentum must equal the net forces. However for fully developed flow the net momentum flux is zero (no accelerations), and hence the forces must sum to zero. The forces involved in the problem are those of pressure and viscosity, and these must be in balance. Therefore

$$\left[\left(p + \frac{dp}{dz}\,dz\right) - p\right] r\,d\theta\,dr = \mu\left[\frac{\partial}{\partial r}\left(\frac{\partial u}{\partial r}\,r\,d\theta\,dz\right)dr + \frac{\partial}{\partial \theta}\left(\frac{1}{r}\frac{\partial u}{\partial \theta}\,dr\,dz\right)d\theta\right] \qquad (1)$$

When one rearranges, the governing equation for the velocity as a function of the coordinates r and θ is obtained:

$$\frac{\partial^2 u}{\partial r^2} + \frac{1}{r}\frac{\partial u}{\partial r} + \frac{1}{r^2}\frac{\partial^2 u}{\partial \theta^2} = \frac{1}{\mu}\frac{dp}{dz} \qquad (2)$$

where the pressure gradient dp/dz is a negative constant. This partial differential equation is frequently called Poisson's equation.

It is not difficult to write a solution of this equation, but subsequently one must face the more challenging task of fitting the solution to the particular boundary conditions of specific problems. The general solution is dealt with here, leaving specific flow situations to later sections.

In approaching Equation (2) it is convenient to introduce a reduced velocity defined by

$$u^* = u - \frac{r^2}{4}\left(\frac{1}{\mu}\frac{dp}{dz}\right) \qquad (3)$$

By substitution into Equation (2) one finds that u^* must obey

$$\frac{\partial^2 u^*}{\partial r^2} + \frac{1}{r}\frac{\partial u^*}{\partial r} + \frac{1}{r^2}\frac{\partial^2 u^*}{\partial \theta^2} = 0 \qquad (4)$$

which is the well-known Laplace equation. The general solution of Equation (4) may be taken from numerous books on advanced calculus. Therefore

$$u^* = A + B \ln r + \sum_{k=1}^{l} (C_k r^k + D_k r^{-k}) \cdot (E_k \cos k\theta + F_k \sin k\theta) \qquad (5)$$

where k takes on integral values to ensure that the velocity is single valued, that is that the velocity computed at a location (r, θ) is identical to that computed at $(r, \theta + 2\pi)$. The constants A, B, etc., in Equation (5) are to be determined from the boundary conditions, as are the number of terms of the series.

Thus a general solution for the velocity is obtained by the combining of Equations (3) and (5) which yields

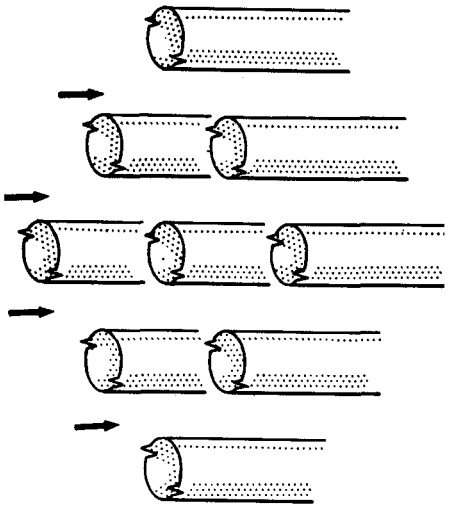

Fig. 1. Schematic of flow configuration.

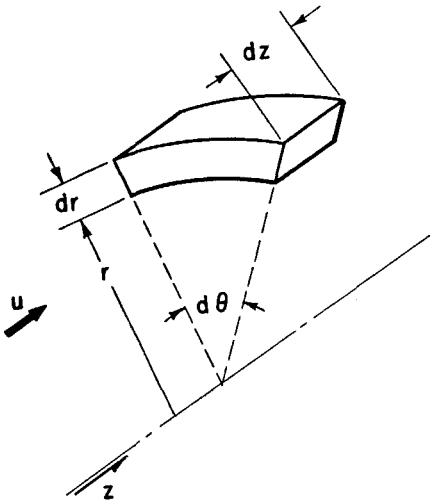

Fig. 2. Control volume for deriving momentum equation.

$$u = A + B \ln r - \frac{r^2}{4}\left(-\frac{1}{\mu}\frac{dp}{dz}\right) + \sum_{k=1}^{l} (C_k r^k + D_k r^{-k}) \cdot (E_k \cos k\theta + F_k \sin k\theta) \qquad (6)$$

Now one may turn to the problem of specializing this solution to flow parallel to cylindrical rods in regular array.

Cylinders in Triangular Array

Consideration is first given to flow between cylinders arranged on centers which form the vertices of equilateral triangles. An end view of the arrangement is shown in Figure 3. From the symmetry of the situation it is easily seen that attention need be focused on only the cross-hatched element in the left-hand sketch. An enlarged view is shown at the right, on which has been noted the boundary conditions and dimensional nomenclature. The condition $\partial u/\partial n = 0$ is the expression of the symmetry property, while the condition that $u = 0$ at the inner boundary stems from the no-slip requirement of viscous flow.

Table 1. Listings of Δ_j and δ_j for Various Spacing Ratios

(a) Values of Δ_j.

s/r_0	Δ_1	Δ_2	Δ_3	Δ_4	Δ_5	Δ_6	Δ_7
4.0	−0.0505	−0.0008	0.0000				
2.0	−0.0505	−0.0008	0.0000				
1.5	−0.0502	−0.0007	0.0000				
1.2	−0.0469	0.0007	0.0002	0.0000			
1.1	−0.0416	0.0028	0.0004	0.0000			
1.05	−0.0368	0.0043	0.0003	−0.0001	0.0000		
1.04	−0.0357	0.0046	0.0002	−0.0001	0.0000		
1.03	−0.0345	0.0049	0.0002	−0.0001	0.0000		
1.02	−0.0332	0.0051	0.0000	−0.0001	0.0000		
1.01	−0.0319	0.0052	−0.0001	−0.0002	0.0000		
1.00	−0.0305	0.0053	−0.0003	−0.0002	0.0000		

(b) Values of δ_j

s/r_0	δ_1	δ_2	δ_3	δ_4	δ_5	δ_6	δ_7
4.0	−0.1253	−0.0106	−0.0006	0.0000			
2.0	−0.1250	−0.0105	−0.0006	0.0000			
1.5	−0.1225	−0.0091	−0.0002	0.0000			
1.2	−0.1104	−0.0024	−0.0015	0.0003	0.0001	0.0000	
1.1	−0.0987	0.0036	0.0029	0.0005	0.0000		
1.05	−0.0904	0.0073	0.0032	0.0002	−0.0001	0.0000	

One may now proceed to apply the boundary conditions to determine the constants of Equation (6). Starting with the simplest conditions, one requires first that $\partial u/\partial n = \partial u/\partial\theta = 0$ at $\theta = 0$ deg. and at $\theta = 30$ deg. From the first of these it follows that since $\cos 0 \neq 0$, then

$$F_k \equiv 0 \qquad (7a)$$

while from the second one finds that

$$k = 6, 12, 18\cdots \qquad (7b)$$

to guarantee that $\sin k\pi/6 = 0$. Next imposing the condition that $u = 0$ at $r = r_0$ one gets

$$D_k = -C_k r_0^{2k},$$

$$A = -B \ln r_0 + \frac{r_0^2}{4}\left(-\frac{1}{\mu}\frac{dp}{dz}\right) \qquad (7c)$$

Further it is required that the total drag force exerted on the fluid by the solid rod be balanced by the net pressure force acting over the entire cross section of the typical element (Figure 3b); that is

$$\int_0^{\pi/6} \mu\left(\frac{\partial u}{\partial r}\right)_{r=r_0} r_0\, d\theta = \int_0^{\pi/6}\int_{r_0}^{s/\cos\theta} \left(\frac{dp}{dz}\right) r\, dr\, d\theta \qquad (8)$$

The evaluation of this over-all force balance from Equation (6) yields

$$B = \frac{\sqrt{3}}{\pi} s^2\left(-\frac{1}{\mu}\frac{dp}{dz}\right) \qquad (7d)$$

Before going on to the final boundary condition the findings of the previous paragraph are brought together, and Equation (6) becomes

$$u = \frac{\sqrt{3}}{\pi} s^2\left(-\frac{1}{\mu}\frac{dp}{dz}\right)\ln\frac{r}{r_0} - \frac{1}{4}\left(-\frac{1}{\mu}\frac{dp}{dz}\right)(r^2 - r_0^2) + \sum_{j=1}^{l} G_j\left(r^{6j} - \frac{r_0^{12j}}{r^{6j}}\right)\cos 6j\theta \qquad (9)$$

where $G_j \equiv C_j E_j$. There still remains the task of determining the G_j, and at one's disposal is the condition that $\partial u/\partial n = 0$ on the right-hand boundary of Figure 3b, on which $r = s/\cos\theta$. It is convenient to make use of the identity

$$\frac{\partial u}{\partial x} = \frac{\partial u}{\partial r}\cos\theta - \frac{\partial u}{\partial\theta}\frac{\sin\theta}{r}$$

where one may associate x with n on the boundary under consideration. Introducing Equation (9) and setting $\partial u/\partial n = 0$ when $r = s/\cos\theta$, one finds after rearrangement

$$\sum_{j=1}^{l} \Delta_j (\cos\theta)^{1-6j}\left[\cos(6j-1)\theta + \left(\frac{r_0\cos\theta}{s}\right)^{12j}\cos(6j+1)\theta\right] + \frac{\sqrt{3}}{\pi}\cos^2\theta - \frac{1}{2} = 0 \qquad (7e)$$

where

$$\Delta_j = G_j \frac{6j\, s^{6j}}{\left(-\frac{1}{\mu}\frac{dp}{dz}\right)s^2} \qquad (7f)$$

Equation (7e) provides a means for determining the Δ_j(that is G_j). The first thought for attacking this equation would be to apply the techniques of Fourier series. Such an approach, if possible, would provide an infinite set of Δ_j while satisfying Equation (7e) at all points along the boundary (that is all $0° \leq \theta \leq 30°$). Unfortunately the nature of Equation (7e) precludes the use of

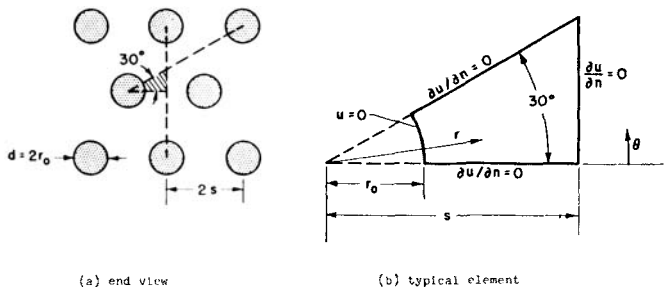

Fig. 3. Diagram of equilateral triangular array.

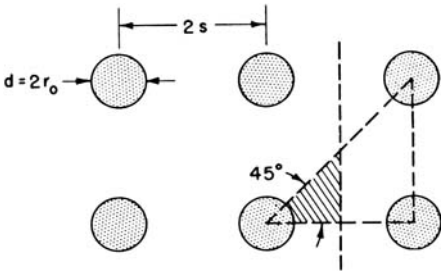

Fig. 4. Diagram of square array.

Fourier analysis, and some other approach must be found for solving for the Δ_j.

The method used here is to apply Equations (7e) at a finite number of points along the boundary. Suppose for example that one successively evaluates Equation (7e) at six values of θ between 0 and 30°. This will provide six equations. If one truncates the series after six terms (that is $l = 6$), then there are sufficient simultaneous equations to evaluate the coefficients $\Delta_1, \Delta_2 \cdots \Delta_6$. This procedure may now be repeated with the use of seven boundary points and seven series coefficients, and so forth. The sets of coefficients Δ_j from these repeated calculations were compared. It was immediately seen that adding additional terms to the series did not significantly affect the numerical values of the first few coefficients. Further it was found that only these first coefficients are important in the computation of the shear stress and velocity distribution. In view of these favorable circumstances the method presented here for determining the Δ_j appears quite adequate.

Numerical values of Δ_j, computed as outlined above, have been listed in Table 1. Inasmuch as the ratio s/r_0 (half spacing to rod radius) appears in Equations (7e), so does it appear as a parameter of Table 1. It is noted that for large spacings (that is large s/r_0) the Δ_j are little affected by increases of spacing, as might have been expected since s/r_0 is raised to a large negative power in Equation (7e). The tabulation is given to four decimal places because this is sufficient for the shear stress and velocity computations.*

So with the determination of the Δ_j (that is, G_j) one may return to Equation (9) and state that the velocity distribution for the triangular array is now available. In a later section the authors will make use of this velocity solution to compute several quantities of engineering interest. But first they will solve for the velocity distribution associated with flow between rods in square array.

Cylinders in Square Array

An end view of the configuration for flow between cylinders in square array is shown schematically in Figure 4. Because of symmetry considerations attention is confined to the cross-hatched element of the sketch. This element has essentially the same form as that shown in Figure 3b, except that now the opening angle is 45 deg. rather than 30 deg. as before.

The velocity solution as given by Equations (6) applies, and one now has to find the constants A, B, $\cdots$ appropriate to the square array. The procedure is identical to that followed in the preceding section for the triangular array. From the conditions that $\partial u/\partial n = \partial u/\partial\theta = 0$ at $\theta = 0$ deg. and $\theta = 45$ deg., there is obtained, respectively

$$F_k \equiv 0 \qquad (10a)$$

and

$$k = 4, 8, 12\cdots \qquad (10b)$$

Imposing the requirement that $u = 0$ at $r = r_0$ gives

$$D_k = -C_k r_0^{2k},$$

$$A = -B \ln r_0 + \frac{r_0^2}{4}\left(-\frac{1}{\mu}\frac{dp}{dz}\right) \qquad (10c)$$

while the over-all force balance between net pressure and wall shear, Equation (8) with $\pi/6$ replaced by $\pi/4$, provides the following value of B:

$$B = \frac{2}{\pi}s^2\left(-\frac{1}{\mu}\frac{dp}{dz}\right) \qquad (10d)$$

Introducing these findings into (6) results in the following equation for the velocity:

$$u = \frac{2}{\pi}s^2\left(-\frac{1}{\mu}\frac{dp}{dz}\right)\ln\frac{r}{r_0} - \frac{1}{4}\left(-\frac{1}{\mu}\frac{dp}{dz}\right)(r^2 - r_0^2) + \sum_{j=1}^{l} G_j\left(r^{4j} - \frac{r_0^{8j}}{r^{4j}}\right)\cos 4j\theta \qquad (11)$$

where the G_j ($= C_j E_j$) still remain to be determined. The condition that $\partial u/\partial n = 0$ on the right-hand boundary of Figure 3b, on which $r = s/\cos\theta$, may be used. The procedure for determining the G_j follows along the lines previously discussed. For several values of θ between 0 and 45 deg. one successively applies the condition of zero normal derivative; that is

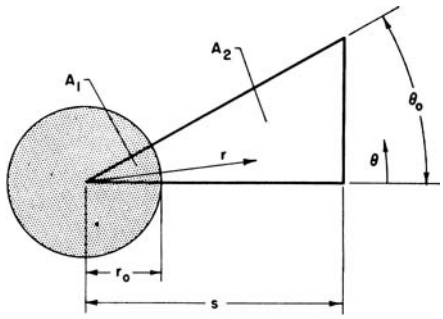

Fig. 5. Diagram for pressure-drop and friction-factor derivation.

$$\sum_{j=1}^{l}\delta_j(\cos\theta)^{1-4j}\left[\cos(4j-1)\theta + \left(\frac{r_0\cos\theta}{s}\right)^{8j}\cos(4j+1)\theta\right] + \frac{2\cos^2\theta}{\pi} - \frac{1}{2} = 0 \qquad (12a)$$

where

$$\delta_j = G_j\frac{4j\,s^{4j}}{\left(-\frac{1}{\mu}\frac{dp}{dz}\right)s^2} \qquad (12b)$$

The result is l simultaneous equations for $\delta_1, \delta_2 \cdots \delta_l$. Sufficient terms are retained in the series to assure good accuracy in shear-stress and velocity-distribution calculations. Numerical values of the δ_j obtained in this manner are listed in Table 1 as a function of s/r_0.

So with the determination of the δ_j (that is G_j) the velocity solution for the square array, Equation (11), can be regarded as known, and one can pass on to the presentation of results of engineering interest.

RESULTS

Attention will first be focused on the pressure drop-flow relationship, which is generally the result of greatest practical importance. Then this information will be rephrased in terms of the friction factor and Reynolds number. Finally plots will be given of velocity contours and also of the distribution of the wall shear stress around the periphery of a rod.

*Additional figures were used in satisfying Equation (7e).

Pressure-Drop–Flow Relationship

First the volume rate of flow Q which may be calculated by integrating the velocity over the flow area is introduced. As before, only a typical element of the flow configuration need be used (Figure 5). In terms of symbols given there the integral for Q becomes

$$Q = \int\int_{A_2} ur\,dr\,d\theta = \int_0^{\theta_0}\int_{r_0}^{s/\cos\theta} ur\,dr\,d\theta \tag{13}$$

In evaluating Equation (13) one introduces u from either Equations (9) or (11) depending whether a triangular or square array is being considered. As is shown in the Appendix the end result of inserting the velocity expressions takes the form

$$Q = \left(-\frac{dp}{dz}\right)\frac{r_0^4}{\mu}\cdot\text{function}\,(s/r_0) \tag{14}$$

or

$$-\frac{dp}{dz} = \frac{Q\mu}{r_0^4}\cdot\frac{1}{\text{function}\,(s/r_0)} \tag{14a}$$

The function of s/r_0 is different for each array and has been computed by the use of the integrals given in the Appendix.

Before numerical results are discussed, an important fact may be drawn from Equation (14a): for a given array with fixed-rod diameter and spacing (that is, fixed configuration) the pressure drop is directly proportional to flow rate. This finding is in accord with previous laminar-flow analyses.

As a final prelude to presenting the pressure-drop results, the authors chose to replace the ratio s/r_0 by the more general variable, the porosity, which is the fraction of the total cross section available to flow. In terms of Figure 5 one may write

$$\epsilon \equiv \frac{A_2}{A_1 + A_2} = 1 - \frac{\theta_0}{(s/r_0)^2\tan\theta_0} \tag{15}$$

where the facts that $(A_1 + A_2)$ is a right triangle and A_1 is a circular sector have been used in deriving the last expression. For the triangular array, $\theta_0 = 30$ deg., and

$$\epsilon = 1 - \frac{\sqrt{3}\pi}{6(s/r_0)^2} \tag{15a}$$

while for the square array, $\theta_0 = 45$ deg., and

$$\epsilon = 1 - \frac{\pi}{4(s/r_0)^2} \tag{15b}$$

With these expressions, plus the evaluated integrals of the Appendix, one is able to plot the pressure-drop–flow relationship as a function of porosity on Figure 6. There are several aspects of the curves worthy of discussion. First it is seen that for the same flow, r_0 and ϵ, the triangular array gives rise to a higher pressure drop. This might have been intuitively expected because each rod in the triangular array is surrounded by more neighbors and hence feels more flow disturbance than does a rod in the square array.

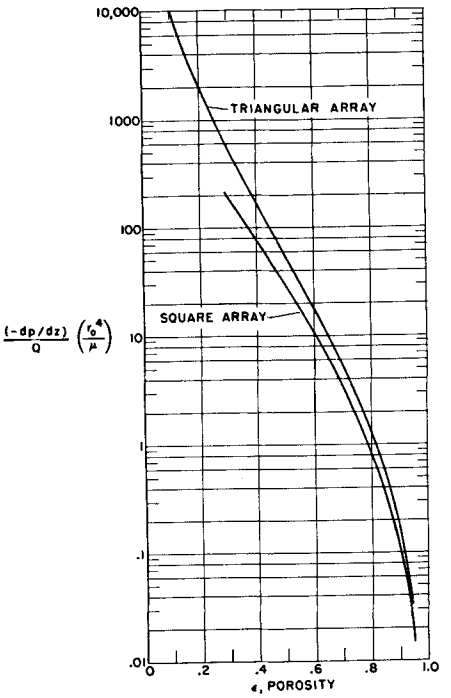

Fig. 6. Pressure-drop–flow parameter as a function of porosity.

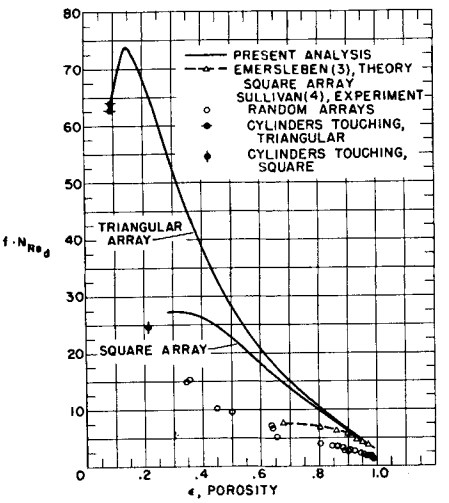

Fig. 7. Friction factor–Reynolds number as a function of porosity.

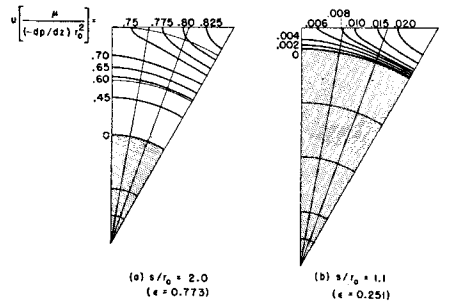

Fig. 8. Representative velocity contour lines for equilateral triangular array.

It would appear that the two curves of the figure have generally the same shape, with possibly a growing deviation at smaller values of ϵ. Consideration of the system suggests that, except for large spacings (large ϵ), similar flow performance need not necessarily be expected from the different arrays. At large spacings, where there is little effect of neighboring rods, the flow passages of the two arrays are almost geometrically similar. But at small spacings the flow passages of the two arrays are very different indeed. For the case of cylinders touching ($s/r_0 = 1$) the passages of the square array are curvilinear squares, and those of the triangular array are curvilinear triangles. One would have no reason to expect that at small spacings the curves for the two arrays should be identical in form. (These observations will have even greater meaning when the friction-factor curves are given.)

That the curves of Figure 6 should give increasing ordinate values with decreasing porosity is intuitively reasonable. If the flow and rod radius are regarded as fixed, and the porosity is decreased, this will give rise to an increase in flow velocity and a decrease in passage dimensions. Both these effects would be expected to contribute to an increase in pressure drop, and this is in accord with the findings of Figure 6.

The rod radius is used here as a characteristic dimension because it can be easily measured and identified in an experiment or application. The equivalent diameter, $\equiv \epsilon d/(1 - \epsilon)$, was also considered but not used because it is physically somewhat obscure in the present instance and did not assist in correlating the results.

Friction-Factor–Reynolds-Number Relationship

The pressure-drop information may be rephrased into a friction-factor–Reynolds-number relationship. To begin, the definition of the friction factor is

$$f \equiv \bar{\tau}\Big/\frac{\rho\bar{u}^2}{2} \tag{16}$$

The shear stress may be related to the pressure drop, dp/dz. When one refers to Figure 5, a force balance yields

$$\bar{\tau}\cdot r_0\theta_0\,dz = -dp\cdot A_2,$$

or

$$\bar{\tau} = -\frac{(dp/dz)A_2}{r_0\theta_0} \tag{17}$$

With this Equation (16) becomes

$$f = -\frac{2(dp/dz)A_2}{r_0\theta_0\rho\bar{u}^2} \tag{16a}$$

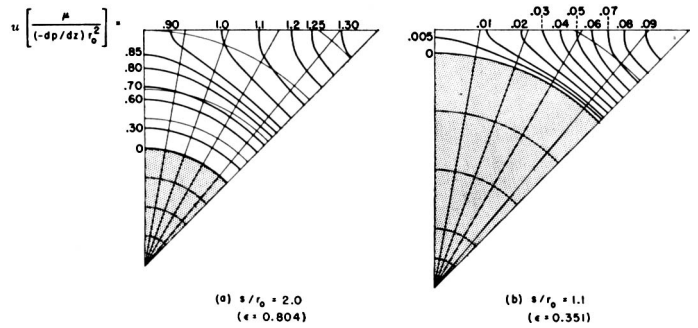

Fig. 9. Representative velocity contour lines for square array.

and, after further rearrangement

$$f \cdot N_{Re_d} = \left[\frac{r_0^4}{Q\mu}\left(-\frac{dp}{dz}\right)\right]\left[\frac{4A_2^2}{\theta_0 r_0^4}\right] \quad (16b)$$

where N_{Re_d} is based on the rod diameter $d(= 2r_0)$ and is given by

$$N_{Re_d} = \frac{d\bar{u}\rho}{\mu}$$

In writing Equation (16*b*) the authors have used the fact that $\bar{u} = Q/A_2$.

The first bracket of Equation (16*b*) is the pressure-drop–flow ratio, which for a given array has been previously shown to depend only on the porosity. The second bracket is purely geometrical. When one uses the definition of ϵ, Equation (15), in conjunction with the geometry of Figure 5, it is easy to show that for a given array the second bracket also is a function of porosity alone.

The friction-factor–Reynolds-number relationship has been computed for each array from Equation (16*b*), and the results are plotted on Figure 7 as a function of porosity. The curve representing the triangular array lies higher than that for the square array, but intuitive interpretation is not easy because, in addition to the pressure drop, complicated geometrical factors enter into the friction factor. For low porosities it would appear that the curves for the two arrays are not completely similar in shape, but, as previously discussed, similarity is not to be expected in the low-porosity range.

For high values of porosity it is possible to find a very accurate analytical representation of the friction-factor results. Under these conditions, where the rods are relatively wide apart, the velocity distribution around any one rod depends very little on the angular position. So the velocity can be accurately represented by the first two terms of Equations (9) and (11). The friction-factor–Reynolds-number relationship corresponding to both these abbreviated velocity expressions is

$$f \cdot N_{Re_d} = \frac{8(1-\epsilon^*)^2}{2\epsilon^* - \ln \epsilon^* - (\epsilon^*)^2/2 - 1.5} \quad (18)$$

where $\epsilon^* = 1 - \epsilon$.

By the comparison of the predictions of this relation with Figure 7 (which is based on the more complete velocity solution) it is found that Equation (18) is an excellent representation of the results for the conditions

$\epsilon > 0.80$, triangular array

$\epsilon > 0.90$, square array

In addition to the curves of the present analysis, Figure 7 also includes the results of related work. The analysis of Emersleben, represented by the triangles* and the dashed line, was carried out for the square array with complex zeta functions used. The nature of his solution is such that it can be valid only for large values of ϵ, but heretofore the actual range of validity has not been known. Inspection of Figure 7 shows that Emersleben's results are in close agreement with those of the current work for $\epsilon > 0.9$, and this may be taken to define the limit of validity of his analysis.

Sullivan's experiments were carried out with parallel-oriented filaments of goat's wool, blond hair, Chinese hair, glass wool, copper wire, and segments of drill rod. Each of these materials was used separately. The tests utilizing the drill rods corresponded to the situation of cylinders touching, and the associated data points are shown as black circles in Figure 7. For the triangular array these data are in excellent agreement with the present predictions and thereby provide support for the theory. For the square array the theory was not carried out for the situation of cylinders touching because of the relatively slower convergence of the truncated series. However inspection of Figure 7 leads to the belief that good agreement would also be obtained for this case. For the other tests (aside from those with the drill rods) the filaments were inserted in a tube in an array which was presumably random. Hence the experimental conditions corresponded to neither of the two regular arrays studied here. The data, shown as open circles in Figure 7, generally fall below the analytical curves. It is especially interesting that the data continue to fall substantially lower than

*The points shown on Figure 7 are those reported by Carman (*2*).

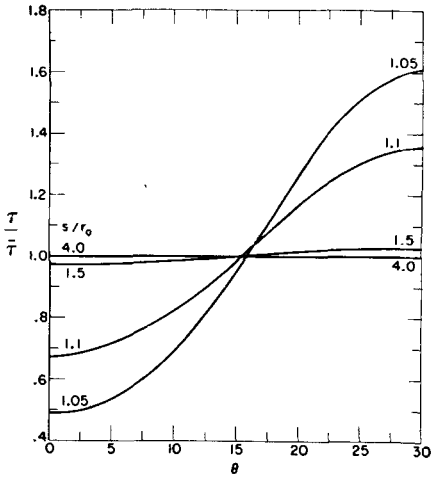

Fig. 10. Local wall shear-stress distribution for equilateral triangular array.

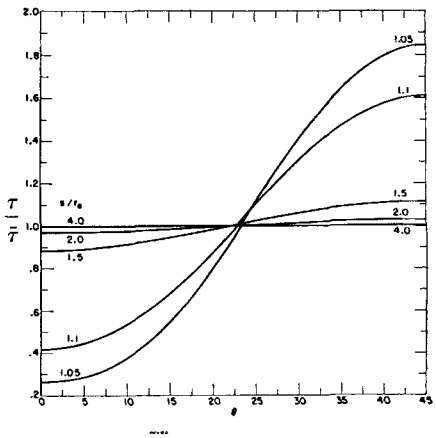

Fig. 11. Local wall shear-stress distribution for square array.

theory even for $\epsilon > 0.9$, where the relatively large spacing essentially removes the effect of rod orientation. This suggests the possibility of a shortcoming in the experimental apparatus, the most likely of which would be that the cylindrical filaments were not tightly packed against the wall of the bounding tube. Such an occurrence would lead to relatively large, open flow areas near walls and a consequent decrease in pressure drop and friction factor.

Velocity Contours

The distribution of the velocity may also be of some interest. The authors have confined themselves to representative situations, selecting results for a spacing ratio s/r_0 of 1.1 to represent close packings and those for a ratio 2.0 to represent open packings. Dimensionless velocity contours (lines of constant velocity) are plotted on Figure 8 for the triangular array for a typical flow element. Inspection of Figure 8*a* (relatively large spacing) reveals that the velocity contours are essentially circular for a sizable region near the rod surface, an indication that the neighboring rods have little effect there. In Figure 8*b*,

where the spacing has decreased, the influence of the neighbors extends to regions very near the rod surface. Similar findings may be observed on the velocity contours of Figures 9*a* and *b* for the square array.

Variation of Local Wall Shear Stress

Since the velocity distribution around a rod varies with angular position, so also will the local shear stress exerted by the wall on the fluid. The manner in which the shear stress varies is shown respectively on Figures 10 and 11 for the triangular and square arrays. Using symmetry considerations as before one need consider only the typical elements which are shown cross hatched in Figures 3 and 4.

The curves of Figures 10 and 11 graphically illustrate the role of neighboring rods on the flow pattern around a given rod. For large spacings, for example $s/r_0 = 4.0$, the local shear stress is essentially a constant around the periphery of the rod, showing that neighbors have little effect on the flow pattern. As the spacing decreases, the angular dependence of the local-wall shear stress increases, testifying to the increasing asymmetry of the flow due to interference of neighbors.

As would be expected on physical grounds the highest shear stress is associated with the location of highest velocities ($\theta = 30$ and 45 deg., respectively), and the smallest shear stress is at the location of lowest velocity ($\theta = 0$ deg.).

CONCLUDING REMARKS

In the investigation reported here the analytical procedure based on truncated trigonometric series has been applied to symmetrical arrays such as the square and the equilateral triangle. However the same methods can be applied with no essential modification to unsymmetrical arrangements, examples of which are the rectangular and the isosceles triangular with various apex angles.

APPENDIX

Integration to Compute Flow Rate

Equation (13) is the integral for the volume flow. For purposes of illustration attention is focused on the square array; the result for triangular array will be given later.

The expression for the velocity for the square array is given by Equation (11). The G_j are related to the tabulated constants δ_j (Table 1) by

$$G_j = \delta_j \frac{(-dp/dz)s^2}{4j\mu s^{4j}} \qquad (A1)$$

For purpose of integration the dimensionless variable

$$\zeta = r/r_0 \qquad (A2)$$

is introduced. Then substituting Equations (11), (A1), and (A2) into the flow-rate integral (13), one gets

$$Q = \left(-\frac{dp}{dz}\right)\frac{r_0^4}{\mu}\left\{\int_0^{\pi/4}\int_1^{s/r_0\cos\theta} \cdot\left[\frac{2}{\pi}\left(\frac{s}{r_0}\right)^2 \ln\zeta - \frac{1}{4}(\zeta^2-1) + \sum_{j=1}^{l}\frac{\delta_j(r_0/s)^{4j-2}}{4j} \cdot(\zeta^{4j} - \zeta^{-8j})\cos 4j\theta\right]\zeta\, d\zeta\, d\theta\right\} \qquad (A3)$$

where $\theta_0 = \pi/4$ has been introduced for the square array. Inspection of the contents of the brace shows that the only parameter is the ratio (s/r_0), ζ being a dummy integration variable. So the assertion of Equation (14) is shown to be correct.

The integrals appearing in Equation (A3) can be carried out in a straightforward way, giving

$$\frac{Q\mu}{(-dp/dz)r_0^4} = \left(\frac{s}{r_0}\right)^4 \cdot\left[\frac{1}{2\pi}\left(2\ln\frac{s}{r_0} + \ln 2 - 3\right) + \frac{1}{6}\right] + \left(\frac{s}{r_0}\right)^4 \sum_{j=1}^{l}\frac{\delta_j}{4j} \cdot\left[\frac{\Lambda_j}{4j+2} + \left(\frac{r_0}{s}\right)^{8j}\frac{\beta_j}{4j-2}\right] + \frac{1}{4}\left(\frac{s}{r_0}\right)^2 - \frac{\pi}{64} \qquad (A4)$$

where

$$\Lambda_j = \int_0^{\pi/4}\frac{\cos 4j\theta}{(\cos\theta)^{4j+2}}\,d\theta,$$

$$\beta_j = \int_0^{\pi/4}\frac{\cos 4j\theta}{(\cos\theta)^{2-4j}}\,d\theta$$

The definite integrals represented by Λ_j and β_j were computed numerically by the Kutta-Runge method.

For the triangular array the authors proceed as above, with the exception that the velocity is taken from Equation (9) with

$$G_j = \Delta_j \frac{(-dp/dz)s^2}{6j\mu s^{6j}} \qquad (A5)$$

The final result for the flow rate for the triangular array is

$$\frac{Q\mu}{(-dp/dz)r_0^4} = \left(\frac{s}{r_0}\right)^4\left[\frac{1}{2\pi}\left(\ln\frac{s}{r_0} - \ln\cos 30^0 - \frac{3}{2}\right) + \frac{13\sqrt{3}}{216}\right] + \left(\frac{s}{r_0}\right)^4 \sum_{j=1}^{l}\frac{\Delta_j}{6j} \cdot\left[\frac{\Omega_j}{6j+2} + \left(\frac{r_0}{s}\right)^{12j}\frac{\chi_j}{6j-2}\right] + \frac{\sqrt{3}}{12}\left(\frac{s}{r_0}\right)^2 - \frac{\pi}{96} \qquad (A6)$$

where

$$\Omega_j = \int_0^{\pi/6}\frac{\cos 6j\theta}{(\cos\theta)^{6j+2}}\,d\theta,$$

$$\chi_j = \int_0^{\pi/6}\frac{\cos 6j\theta}{(\cos\theta)^{2-6j}}\,d\theta$$

NOTATION

A,B,C,D,E,F,G = constants in velocity solution
A_1 = solid area normal to flow direction
A_2 = flow area
d = cylinder diameter, $2r_0$
f = friction factor, $2\bar{\tau}/\rho\bar{u}^2$
n = direction of the normal
N_{Re} = Reynolds number, $d\bar{u}\rho/\mu$
p = static pressure
Q = volumetric rate of flow through typical element (See Figures 3*a* and 4.)
r = radial coordinate measured from center of cylinder
r_0 = cylinder radius
s = half spacing between cylinders
u = velocity in $+z$ direction
u^* = reduced velocity defined by Equation (3)
$\bar{u}$ = mean velocity
z = longitudinal coordinate

Greek Symbols

δ_j = constants defined by Equation (12*b*)
Δ_j = constants defined by Equation (7*f*)
ϵ = porosity, $A_2/(A_1 + A_2)$
ϵ^* = solidity, $1 - \epsilon$
ρ = fluid density
θ = angular coordinate
θ_0 = angle subtended by flow element
τ = shear stress at cylinder wall
$\bar{\tau}$ = average shear stress
μ = fluid viscosity

LITERATURE CITED

1. Hawksley, P. G. W., "The Effect of Concentration on the Settling of Suspensions and Flow through Porous Media: Some Aspects of Fluid Flow," pp. 114 to 135, Edward Arnold and Co., London (1951).
1a. *Ibid.* p. 132.
2. Carman, P. C., Flow of Gases through Porous Media," Butterworth Science Publishers, London (1956).
2a. *Ibid.*, pp. 26–28.
3. Emersleben, Otto, *Physik. Z.*, Bd. 26, 601 (1925).
4. Sullivan, R. R., *J. Appl. Phys.*, **13**, 725 (1942).

Manuscript received October 27, 1958; paper accepted January 21, 1959.